Chapter V

Design and Development of Electrochemical Immunosensing Platform for the detection of Human Serum Albumin

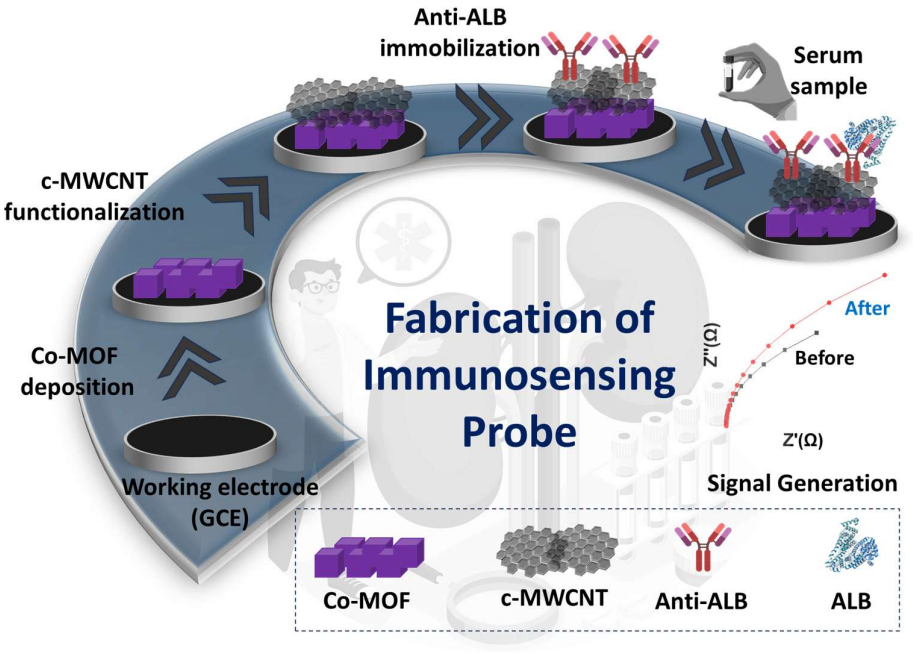

Divya *et. al,* ***IEEE Sensors 2023, 1-4***

Divya et. al, ***Applied Organometallic Chemistry 2025, Vol. 39***

1. Introduction

MOF is an emerging class of materials that is crystalline, porous, three-dimensional, and highly structured in nature [1]. Its constituents self-assemble into a range of 2D or 3D structures, including organic linker moieties like amines, carboxylates, or imidazolates and inorganic metal ions like cobalt, zinc, or copper [2,3]. Thus, MOFs epitomize the elegance of chemical structures that unite organic molecules (linkers) and inorganic metal ions together in a single structure. These materials' large surface area, adjustable pore and channel size, and ease of functionalization have garnered a lot of interest [4,5]. They hold tremendous potential for applications in the healthcare, energy, and environmental sectors owing to their fine-tuning properties [6–8]. MOFs are categorized into a variety of subclasses, the ZIF subclass being one of them where imidazolyl ligands interact with transition metal ions to produce tetrahedral ZIFs [9,10]. Among several ZIFs, ZIF-67 (Co-MOF) stands out as a most widely used material because of its facile synthesis procedure, enormous surface areas, enhanced adaptability, and exceptional mechanical, chemical, and thermal stability [4,11]. The preparation of Co-MOF typically entails a self-assembly process involving the cobalt metal ion (Co^{2+}) and the 2-methylimidazole linker, where the linker moiety serves as the bridging unit that links the Co^{2+} centers [4]. Co-MOF has a broad range of utility, such as catalysis, energy storage, gas adsorption, drug delivery, sensing, and as antibacterial agents [12–14]. The presence of Co^{2+} facilitates the reduction or oxidation of target molecule which boosts sensor performance due to which Co-MOF is at the forefront among all ZIFs for fabrication of electrochemical sensors. However, as Co-MOF lacks stability in aqueous solutions and has limited electrical conductivity in its pristine form [15], it is essential to incorporate conductive materials into Co-MOF matrices. MWCNTs, a class of carbon nanomaterials, are frequently employed as electrode materials because of their intrinsic properties, which include high adherence to the electrode surface and good electrical conductivity [16]. Because of their π conjugate structure,

it can interact with organic linker moiety more effectively through π-π bonding, which results in accelerated electron transfer and an amplified signal [11,17,18]. Moreover, immobilizing antibodies on the surface of electrodes can enhance the specificity and selectivity of the c-MWCNT/Co-MOF composite for the detection of harmful target analytes.

Human Serum Albumin (ALB) is the most abundant protein in plasma, where it performs a multitude of physiological functions and is also employed as a biomarker for a number of diseases [19,20]. ALB levels in the urine of normal adults should not exceed 30 mg/L, and serum levels should range from 35 to 50 mg/mL [19]. Its levels and function are particularly important in the context of kidney disease. Growing research has shown that damage to the kidneys increases ALB leakage into the urine, leading to even potentially fatal conditions such as chronic kidney disease [19,21,22]. Therefore, it is imperative to develop an effective platform for precise ALB tracking with a lower limit of detection in complex matrices. A variety of techniques, including radioimmunoassay, high-performance liquid chromatography, immunonephelometric, and fluorescence immunoassays, are currently employed in clinics for screening of ALB [23-24]. Nevertheless, the majority of these technologies are tedious, require advanced technology, and competent individuals for performing tests [23,25,26]. Therefore, there is an urgent need for facile point-of-care immunosensing system that have the capability to quickly and selectively detect ALB in the clinically relevant range.

In light of this, we have employed c-MWCNT and Co-MOF as electrode materials to produce a novel nanohybrid, immobilized the anti-ALB antibody by carbodiimide bioconjugation, and investigated the potential applications of the platform for ALB detection. The porous nature of Co-MOF and the enormous surface area of c-MWCNT and Co-MOF offered a multitude of active sites for antibodies' functionalization. Further, enhanced sensitivity was achieved in the presence of target antigen due to the combined effects of Co-

MOF catalytic characteristics and MWCNTs' fast electron transfer characteristic. Each step of the probe was accessed using physical characterization techniques including SEM, XRD, XPS, XRD and electrochemically tested by cyclic voltammetry (CV) and electrochemical impedance spectroscopy (EIS). Following that, the sensing probe was tested for its ability to detect ALB in the presence of the redox mediator $Fe(CN)_6^{3-/4-}$, also referred to as Zobell's solution (ZS). The current response on the sensing surface reduced as the concentration of antigen was raised; thus, it serves as a label-free sensor system for ALB analytes. We then evaluated the sensor's capacity to detect ALB specifically in the presence of co-interfering molecules. This immunosensing device is the first of its kind to use Co-MOF-c-MWCNT nanohybrid for the prompt, facile, and targeted detection of kidney dysfunction. **Figure 5.1** depicts the synthesis of Co-MOF and the fabrication of the label-free immunosensing probe for the detection of ALB.

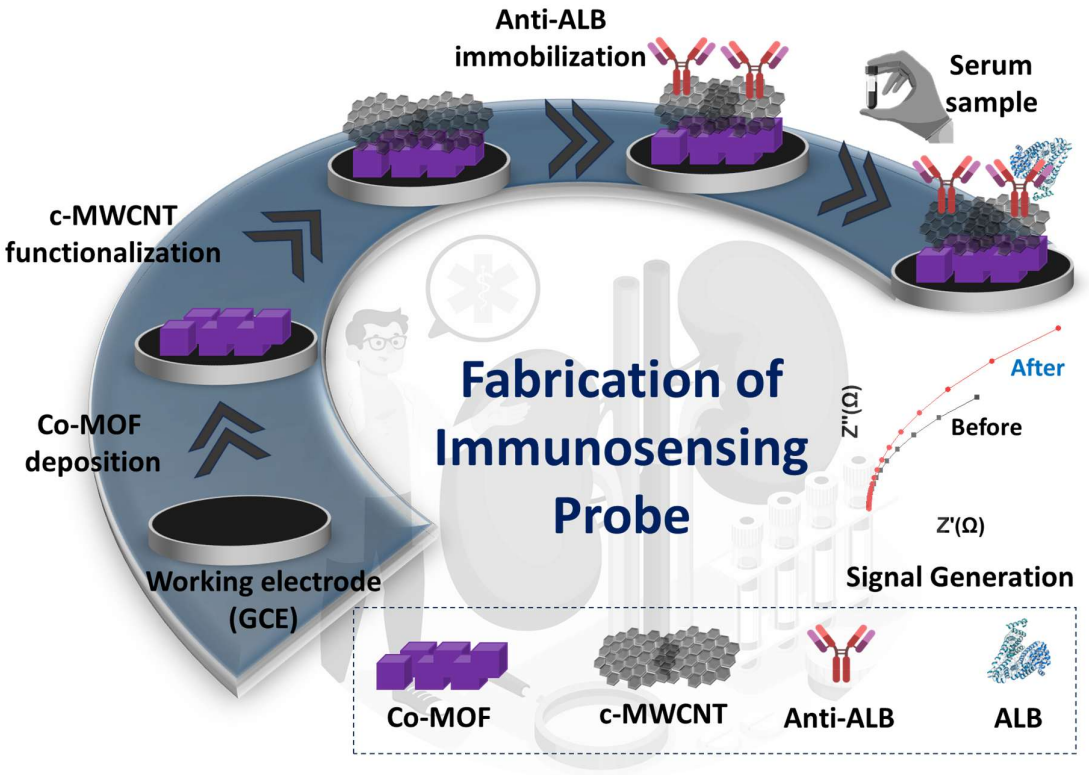

Figure 5.1: *Illustration of step-by-step procedure for the fabrication of a final sensing probe and its deployment in the sensing of ALB in a serum sample*

2. Experimental Section

2.1 Materials and Methods

Cobalt nitrate hexahydrate ($Co(NO_3)_2.6H_2O$), 2-Methylimidazole (MeIm), potassium ferrocyanide ($K_4Fe(CN)_6.3H_2O$), potassium ferricyanide ($K_3Fe(CN)_6$), sodium chloride (NaCl), sodium phosphate monobasic (NaH_2PO_4), 1-(3 dimethylaminopropyl) 3-ethyl carbodiimide hydrochloride (EDC), n-hydroxysuccinimide (NHS), sodium phosphate dibasic (Na_2HPO_4), glucose, glutamine, ascorbic acid, creatinine, globulin, lysozyme, uric acid, cysteine, and human serum albumin (HSA) were procured from SRL research laboratory, India. Standard serum (RM 1112) was procured from Hi-Media, Maharashtra, India. The antibodies against HSA (anti-ALB) were procured from Santa Cruz Biotechnology, Inc. Methanol was procured from Merck Millipore. Distilled water (Milli-Q) was used throughout the experiment. 0.1 M phosphate buffer saline (PBS) (pH - 7.4) was prepared using the established method and used in further experiments.

2.2 Instrumentation

Fourier Transform Infrared Spectroscopy (FTIR) (Nicolet iS5, THERMO Electron Scientific Instruments LLC) was used to study the changes in functional groups occurring after successive synthesis steps. The spectra were obtained through transmittance mode. Morphological study of the synthesized material was performed using Scanning Electron Microscope (SEM) (EVO - Scanning Electron Microscope MA15/18, CARL ZEISS MICROSCOPY LTD., Oxford Instruments Nanoanalysis). Further, elemental analysis was performed using Energy dispersive X-ray spectroscopy (EDS) (Team Pegasus Integrated EDS-EBSD with Octane Plus and Hikari Pro, EDAX Inc.). X-ray photoelectron spectroscopy (XPS) (K-Alpha, Thermo Fisher Scientific) was performed for the analysis of the elemental oxidation state present in the material. X-ray diffraction (XRD) was conducted using a Bench-Top XRD (Rigaku Miniflex

600 Desktop X-Ray Diffraction System, RIGAKU Corporation) where the materials were scanned in the 5°- 80° range at a 5°/min scan rate and 0.01° step size.

2.3 Preparation of the Immunosensor

Initially, Co-MOF was synthesized using a previously reported method[27][28], with minor modifications. In the first step, 0.6 g of cobalt nitrate hexahydrate and 1 g 2-methylimidazole were dissolved separately in 25 ml of methanol solution. After that, 2-methlyimidazole solution was dropwise added to the solution of cobalt nitrate hexahydrate with constant stirring and the color change from orange to purple was observed. The mixture was stir using magnetic stirrer at 280 rpm for 30 mins and then the solution was placed at a room temperature in static mode for 24 hrs. In the final step the solution was centrifuged and washed with methanol three times and the obtained purple precipitate was allowed to dry overnight at 70º C. The obtained powder was stored in the desiccators and used for further experimentation. After synthesis of Co-MOF, the sensor matrix was designed through stepwise modifications of the working electrode surface, i.e., the glassy carbon electrode (GCE) surface. In the first step of the fabrication, 4 µL of Co-MOF (0.5 mg/mL) was coated on the bare electrode and was allowed to dry for 20 minutes. In the subsequent step, 5 µL of c-MWCNTs was drop-coated on the Co-MOF/GCE modified electrode surface and left to dry at room temperature for 20 minutes. Further, for the immobilization of anti-ALB, the dried c-MWCNT/Co-MOF/GCE surface was activated using 10 µL of EDC-NHS solution (100:100 mM) and was allowed to react for 25 minutes. Following the incubation, the EDC-NHS treated surface was washed with PBS buffer to remove the unbound molecules. In the next step, 4 µL of anti-ALB was drop-coated onto the activated c-MWCNT/Co-MOF/GCE surface and kept for an incubation period of 2 hours at optimum temperature. To get rid of any leftover unattached antibody molecules, the anti-ALB/c-MWCNT/Co-MOF/GCE sensing surface that had been developed was washed with PBS.

Finally, 5 μL of 1% BSA was employed to block unspecific binding sites on the sensing surface. Step-by-step development of the immunosensor is depicted in **Figure 5.1**.

2.4 Electrochemical Measurement

Electrochemical analyses were performed using a potentiostat (Palm Sens) connected with a three-electrode system consisting of platinum wire as a counter, an Ag/AgCl electrode as a reference, and GCE as a working electrode, respectively. CV was conducted in the range of -0.4 to +0.8 V vs Ag/AgCl and at a scan rate of 50 mV/s in 5 mM Zobell's solution (ZS). The analytical feasibility of the sensing surface was determined employing EIS with 10 mV amplitude alternating between the frequency range of 10,000 to 0.05 Hz. The impedance values were correlated with an analogous Randles circuit simulation using PS Trace software.

2.5 Real Sample Preparation

The designed sensing probe's effectiveness has been confirmed utilizing a serum sample as the real sample. In order to assess the efficiency of the probe in detecting ALB, a traditional spike and recovery model was utilized. After being equilibrated ten times in PBS, serum samples were spiked with different ALB concentrations. The current outcome has been noted and compared to the standard plot derived at various ALB concentrations in a standard buffer solution.

3. Results and Discussion

3.1 Physical Characterization

At first, SEM was performed to predict the morphology and ensure the proper synthesis of Co-MOF. **Figure 5.2(a-b)** represents the SEM images of Co-MOF showing the cuboidal structure of the synthesized MOF, which was confirmed from the previously reported studies [29,30]. Additionally, EDX was performed for elemental analysis of the Co-MOF, and the presence of Co was confirmed with an atomic percentage of 2.1, along with C and N, which are around 52.5 and 45.4 %, respectively.

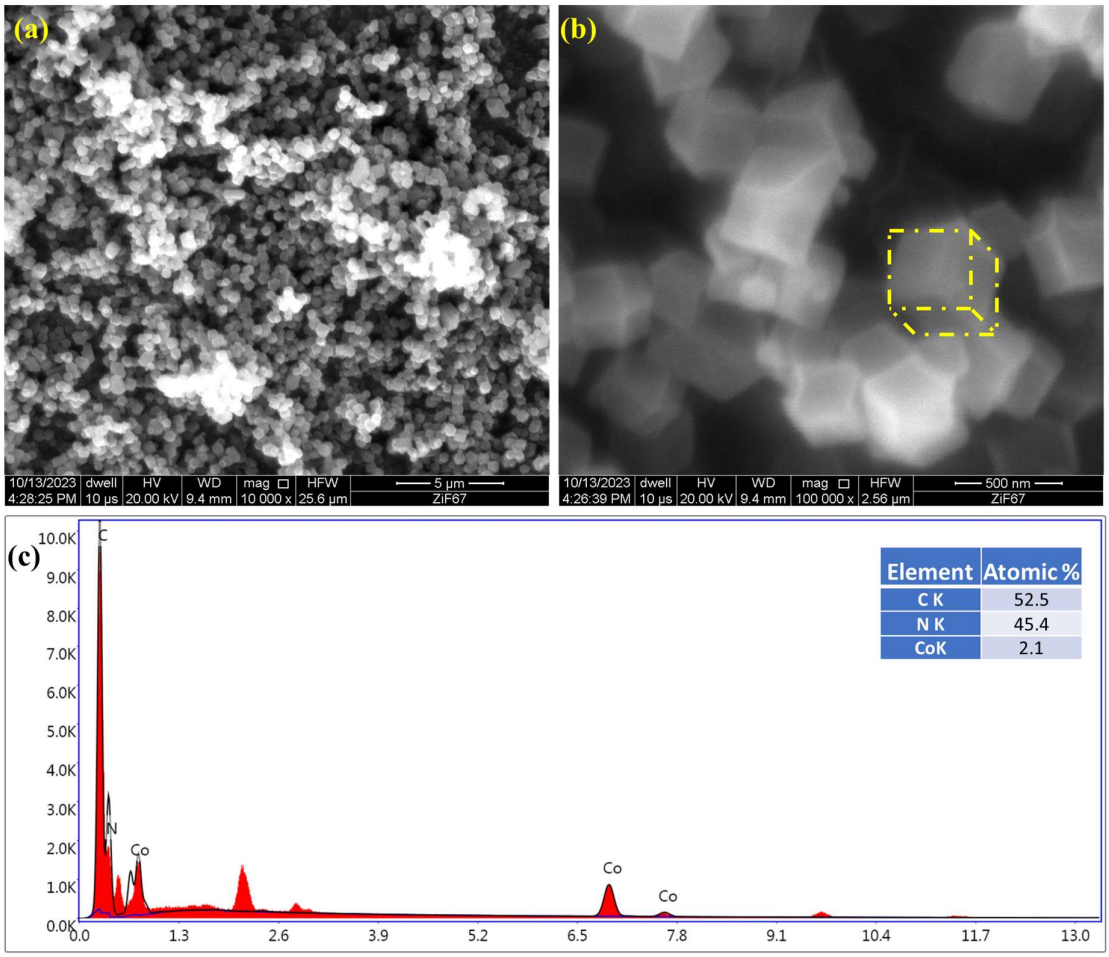

Figure 5.2: (a) *SEM image of synthesized Co-MOF at 5 µm scale,* ***(b)*** *magnified image at 500 nm scale,* ***(c)*** *EDS spectrum of Co-MOF (inset: table representing the atomic % of each element)*

Further, to provide detailed structural information of our nanocomposite, we further performed XRD analysis of Co-MOF, c-MWCNT, and c-MWCNT/Co-MOF nanocomposite. **Figure 5.3(a)** depicts the XRD pattern of Co-MOF where characteristic diffraction peaks at various 2θ values corresponds to its crystallinity were observed. The peaks appeared at 7.36, 10.46, 12.83, 16.52, 17, 18.10, 22.16, 24.48, and 26.74 corresponding to the 011, 002, 112, 022, 013, 222, 114, 233, and 134 crystal planes (COD ref. Card:7222297). These peaks validate the successful synthesis and demonstrate Co-MOF crystalline nature, in line with previously published literature [31]. Further, the XRD analysis represented in **Figure 5.3(b)** shows the strong diffraction at about 26°, which corresponds to the (002) crystallographic plane, strongly

demonstrated the c-MWCNT's crystalline structure. It depicts the d-spacing, or interlayer spacing, that exists between the graphitic layers inside the nanotubes. In addition, there is also a less prominent peak at about 43° corresponding to the (100) crystal plane, which indicates the in-plane ordering of carbon atoms(JCPDS # 96-101-1061)[32][33]. **Figure 5.3(c)** represents the pattern of the nanocomposite which exhibited peaks corresponding to both MWCNT and crystalline Co-MOF, confirming the successful formation of the composite. Variations in peak position or intensity compared to pure components might suggest interactions with them.

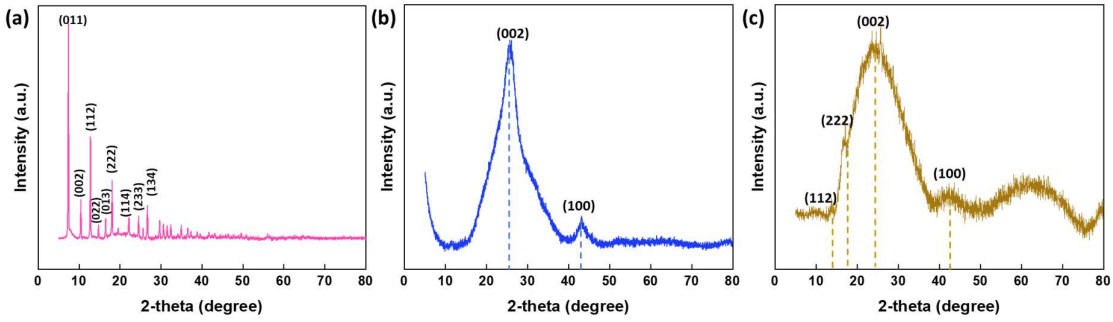

Figure 5.3: *XRD graph of* ***(a)*** *Co-MOF,* ***(b)*** *c-MWCNT,* ***(c)*** *c-MWCNT/Co-MOF with their signature peaks depicting the crystalline structure of the synthesized material*

After studying about the morphology, crystallinity, and elemental analysis of the synthesized materials, XPS was performed in order to provide a more comprehensive understanding of the oxidation states/binding states of the characterized elements at each step of the fabrication**.** **Figure 5.4(a)** represents the complete spectra from 0 to 1400 eV binding energy of all the elements present in Co-MOF, c-MWCNT, and c-MWCNT/Co-MOF nanocomposite. The % of all the elements present in individual and composite material are represented in **Table 5.1**. The individual peaks were studied for each element, and the peaks are deconvoluted for more clear presentation and understanding.

Table 5.1: *Representation of the % of elements presents in every modified surface obtained from XPS*

Modified Surface	Atomic % (C)	Atomic % (O)	Atomic % (N)	Atomic % (Co)
Co-MOF	78.87	0	11.92	9.2
c-MWCNT	41.04	58.96	0	0
c-MWCNT/Co-MOF	48.13	33.07	9.6	9.2

Figure 5.4(b) displayed the C1s spectra where two distinct peaks at 284.36 and 285.39 eV were observed, signifying the C-N and C=C, respectively. **Figure 5.4(c)** represents the N1s spectra, where three different peaks were observed at 398.53, 398.72, and 400.38 eV, which account for the C-N, C-N, and C=N bonds present in the material, respectively. **Figure 5.4(d)** shows the Co2p peaks, with the signature peaks at 781.01 and 796.78 eV representing the Co $2p_{3/2}$ and Co $2p_{1/2}$ spin orbits, respectively. In addition to these, the satellite (Sat.) peaks of Co $2p_{3/2}$ and Co $2p_{1/2}$ were also reported at 785.11 and 801.90 eV, respectively. The similar peaks were also reported earlier, hence confirming the proper synthesis of Co-MOF [34,35]. These peaks were confirmed with the previous studies establishing the synthesis of Co-MOF [36,37]. **Figure 5.4(e-f)** represents the XPS spectra of C1s and O1s of c-MWCNT where the presence of peaks at 284.3 and 285.97 eV represents the C-O and C=C in C1s spectra and peak at 581.98 corresponds to C-O bonds in O1s spectra, respectively, represents the bonds present in sheet structure of c-MWCNT. After that, XPS of the MWCNT/Co-MOF was performed and the C1s, N1s, O1s, and Co2p were plotted in **Figure 5.4(g-j)** which confirms the synthesis of nanocomposite. The C-O peaks in O1s spectra represent the signature peaks, C-N, C=C peaks in C1s spectra and Co2p spectra with the signature peaks at 781.01 and 796.78 eV representing the Co $2p_{3/2}$ and Co $2p_{1/2}$ spin orbits, respectively. All these peaks were signature representative of presence of peaks in the subsequent structures.

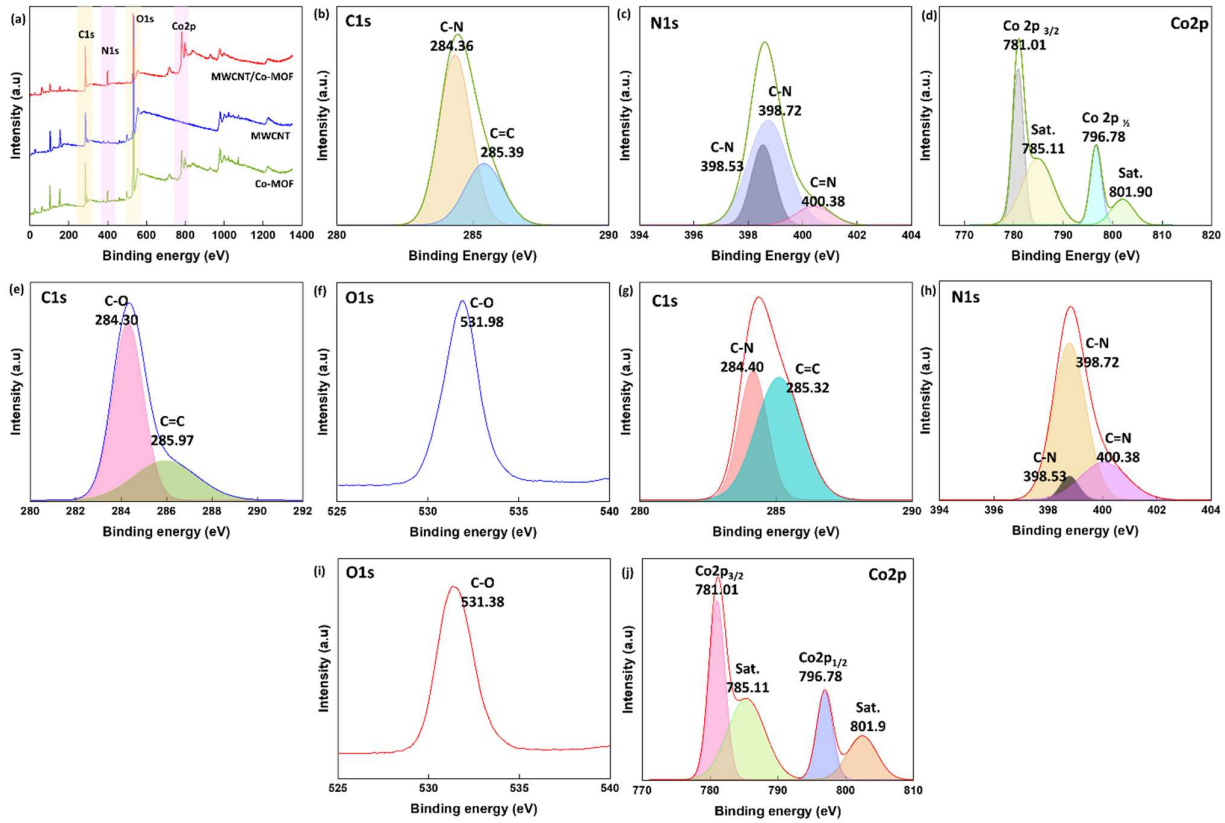

Figure 5.4: *XPS spectra of* ***(a)*** *all the elements present in Co-MOF, MWCNT, and MWCNT/Co-MOF,* ***(b)*** *C1s peak,* ***(c)*** *N1s peak, and* ***(d)*** *Co2p peaks of Co-MOF (represented with green peaks as shown in complete spectra),* ***(e)*** *C1s and* ***(f)*** *O1s of MWCNT (represented with blue peaks as shown in complete spectra),* ***(g)*** *C1s,* ***(h)*** *N1s,* ***(i)*** *O1s, and* ***(j)*** *Co2p peaks of MWCNT/Co-MOF (represented with the red peaks as shown in complete spectra)*

After confirming the elemental composition and the oxidation states of the elements present in synthesized Co-MOF, FTIR was performed to analyze the bond formation and functional groups present in the subsequent modified surfaces. The peaks observed for Co-MOF in **Figure 5.5(i)** between 600 and 1500 cm^{-1} represent the stretching and bending vibrations of the imidazole ring present in its chemical structure. The peaks observed at 1306, 1450, and 2945 cm^{-1} represent the C-N, C=N bonds of 2-methyl imidazole, and C-H bonds of the imidazole ring, respectively. **Figure 5.5(ii)** represents the FTIR curve of c-MWCNT, where peaks at 1445 cm^{-1}, 1644 cm^{-1}, 3248 cm^{-1} show the C=C, C=O, and OH group present in the structure contributing to the successful synthesis of c-MWCNT on the Co-MOF/GCE surface. The peaks

observed in **Figure 5.5(iii)** represent the spectra of the c-MWCNT/Co-MOF/GCE modified surface, where the prominent peak of the C=O group near 1600 cm^{-1}, C=N near 1450 cm^{-1}, and O-H bonds at 3248 cm^{-1} were observed. Further, in the spectra after antibody (anti-ALB) immobilization over the c-MWCNT/Co-MOF/GCE, the additional signature peaks of amide I and amide II were observed in **Figure 5.5(iv)** at 1651 cm^{-1} and 1538 cm^{-1}, respectively, which represent the bond formation after anti-ALB immobilization, stating the synthesis of the final anti-ALB/c-MWCNT/Co-MOF/GCE sensing probe.

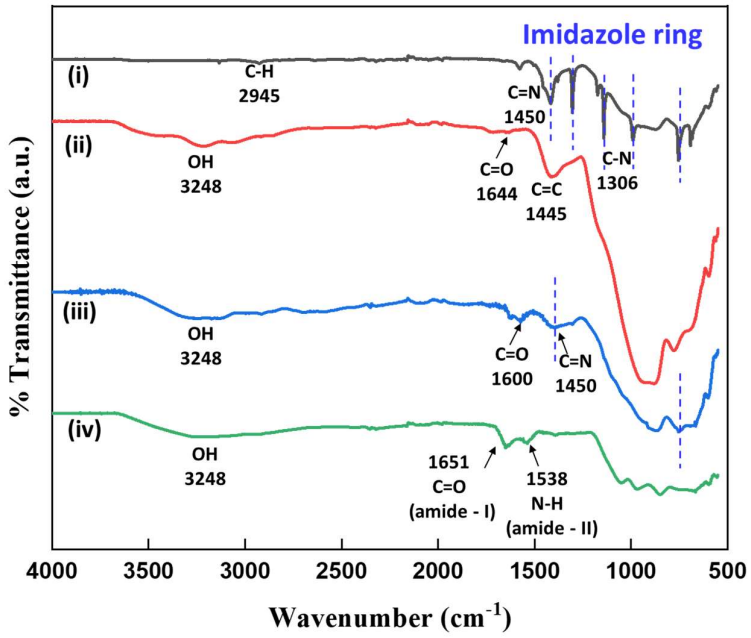

Figure 5.5: *FTIR spectra of* ***(i)*** *Co-MOF,* ***(ii)*** *c-MWCNT,* ***(iii)*** *c-MWCNT/Co-MOF, and* ***(iv)*** *anti-ALB/c-MWCNT/Co-MOF*

3.2 Electrochemical Characterization

The sensing probe's fabrication has been characterized by employing electrochemical methods, viz. CV and EIS in 5 mM ZS. CV responses of bare GCE (pink), Co-MOF/GCE (green), c-MWCNT/Co-MOF/GCE (yellow), and anti-ALB/c-MWCNT/Co-MOF/GCE (blue) are represented in **Figure 5.6(a)**. When Co-MOF was drop casted on the interface of the electrode, a decrease in peak current was seen, confirming the Co-MOF/GCE surface's formation. This

decrease in current was due to poor conductivity possessed by the MOF, similar to previously reported articles [38,39].

Further after the deposition of c-MWCNT on the Co-MOF/GCE surface, the increase in current was observed, which represents the conductive behaviour of c-MWCNT and confirms the synthesis of c-MWCNT/Co-MOF/GCE. This surge in current also represents the increased surface area, which eventually helps in increased charge transfer. Finally, after the immobilization of antibody (anti-ALB), a reduction in current values was seen, which was attributed to the insulating behaviour of the antibody molecule, and this decrease also confirms the successful fabrication of the final anti-ALB/c-MWCNT/Co-MOF/GCE sensing probe. **Figure 5.6(b)** depicts the representative anodic and cathodic peak currents of each modified surface as a histogram.

In addition to CV, EIS was also performed for every subsequent step, and the obtained Nyquist plots for bare GCE (pink), Co-MOF/GCE (green), c-MWCNT/Co-MOF/GCE (yellow), and anti-ALB/c-MWCNT/Co-MOF/GCE (blue) are represented in **Figure 5.6(c)**. Rct represents charge transfer resistance, and it was calculated by fitting the Randles circuit fitting through EIS spectra. It is often calculated through the diameter of the semicircle in the Nyquist plot, and the bigger semicircle implies a higher charge transfer resistance, which indicates the slower electron kinetics. The calculated charge transfer resistance (Rct/R2) using Nyquist plots for bare GCE, Co-MOF/GCE, c-MWCNT/Co-MOF/GCE, and anti-ALB/c-MWCNT/Co-MOF/GCE were found to be 310.0 ± 9.9 Ω, 519.7 ± 17.6 Ω, 404.3 ± 9.5 Ω, and 712.4 ± 14.9 Ω, respectively. The Rct values for modified surfaces, corroborating with CV results, are also shown as histograms in **Figure 5.6(d)**.

Further for establishing the effect of the surface area of the electrode on the electron transfer, the Randles Sevcik equation **(equation 1)** was used to calculate the area after each modification until antibody immobilization.

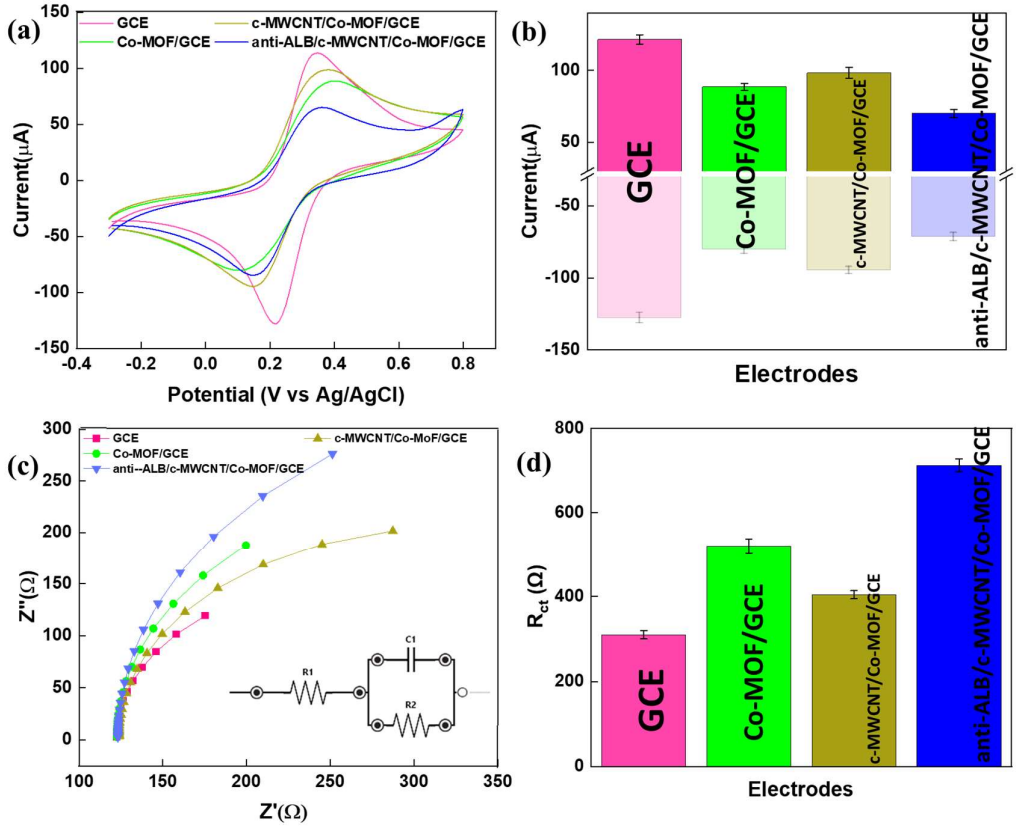

Figure 5.6: ***(a)*** *CV responses of bare GCE (pink), Co-MOF/GCE (green), c-MWCNT/Co-MOF/GCE (yellow), and anti-ALB/c-MWCNT/Co-MOF/GCE (blue) electrodes in 5 mM ZS;* ***(b)*** *histogram showing the respective anodic and cathodic current output;* ***(c)*** *EIS responses of bare GCE (pink), Co-MOF/GCE (green), c-MWCNT/Co-MOF/GCE (yellow), and anti-ALB/c-MWCNT/Co-MOF/GCE (blue) electrode surfaces (inset: equivalent Randles circuit; where R1, C1, and R2 represent the solution resistance, double layer capacitance, and charge transfer resistance, respectively);* ***(d)*** *histogram displaying the corresponding Rct values that were derived from the Nyquist plot*

This facilitates the comparison of the electrocatalytic activity and charge transfer of the subsequent modified surfaces.

$$I_p = 2.69 \times 10^5\, n^{3/2} A C D^{1/2} v^{1/2} \qquad \text{equation 1}$$

where, I_p: peak current (A); n: number of electrons transferred in a redox reaction [in this work, n=1]; D: diffusion coefficient (cm^2/s); A: effective surface area (cm^2); C: concentration of the electroactive species ($mole/cm^3$); v: scan rate in V/s.

The calculated area was found to be 0.15, 0.11, 0.12, and 0.08 cm^2 for GCE, Co-MOF/GCE, c-MWCNT/Co-MOF/GCE, and anti-ALB/c-MWCNT/Co-MOF/GCE, respectively.

Further, a scan rate study was also conducted for the final anti-ALB/c-MWCNT/Co-MOF/GCE sensing surface to examine the processes at the electrode/electrolyte interface by performing CV with varying scan rates from 10 to 100 mV/s, and the obtained curves are depicted in **Figure 5.7(a)**. The observed anodic and cathodic current output were plotted against the square root of scan rate as depicted in **Figure 5.7(b),** and there was a direct proportionality of current with square root of scan rate as discussed in the Randles Sevcik equation. The obtained linear regression curve clearly suggests diffusion-controlled process at electrode/electrolyte interface. The steadily rise in the current value following an increment in scan rate also signifies the stability of the sensing probe. This stability was provided by the Co-MOF as it helps in adhesion of c-MWCNT over the electrode surface without the need for binding agent and it also provide larger surface area for the antibody molecules. Hence, the incorporation of Co-MOF plays an important role in the development of final sensing probe the detection of target molecule.

3.3 Analytical Performance

The immuno-complexation capability of the anti-ALB/c-MWCNT/Co-MOF/GCE sensing probe was initially assessed by allowing the ALB to react for 30 minutes with the final surface. After the incubation period, the ALB/anti-ALB/c-MWCNT/Co-MOF/GCE surface was washed with PBS to remove any unbound ALB, and then the EIS signal was recorded. The increment in Rct value validates the successful reaction between the target analyte and the sensing probe. The obtained EIS spectra of different concentrations are represented in **Figure 5.7(c),** and it was noted that an increase in Rct was recorded with an increase in concentrations of ALB. This rise has been attributed to immuno-complexation on the electrode surface, which prevents transfer of charge, resulting in an increase in the Rct values. **Figure 5.7(d)** illustrates

the calibration plot that was generated using the findings of the EIS study's concentration-dependent responses. The obtained linearity for ALB was found to be 0.1 to 60 mg/mL, covering the clinically important ranges. The limit of detection (LOD) was calculated using LOD = 3.3 SD/slope (m) and found to be 0.024 (±0.001) mg/mL. The obtained linear regression equation is represented as ΔRct (Ω) = 12.84 (±5.21) x [conc. of ALB] + 10.47 (±0.67). The inclusive range of ALB concentrations shows the potential of the developed sensing surface for the diagnosis of renal diseases.

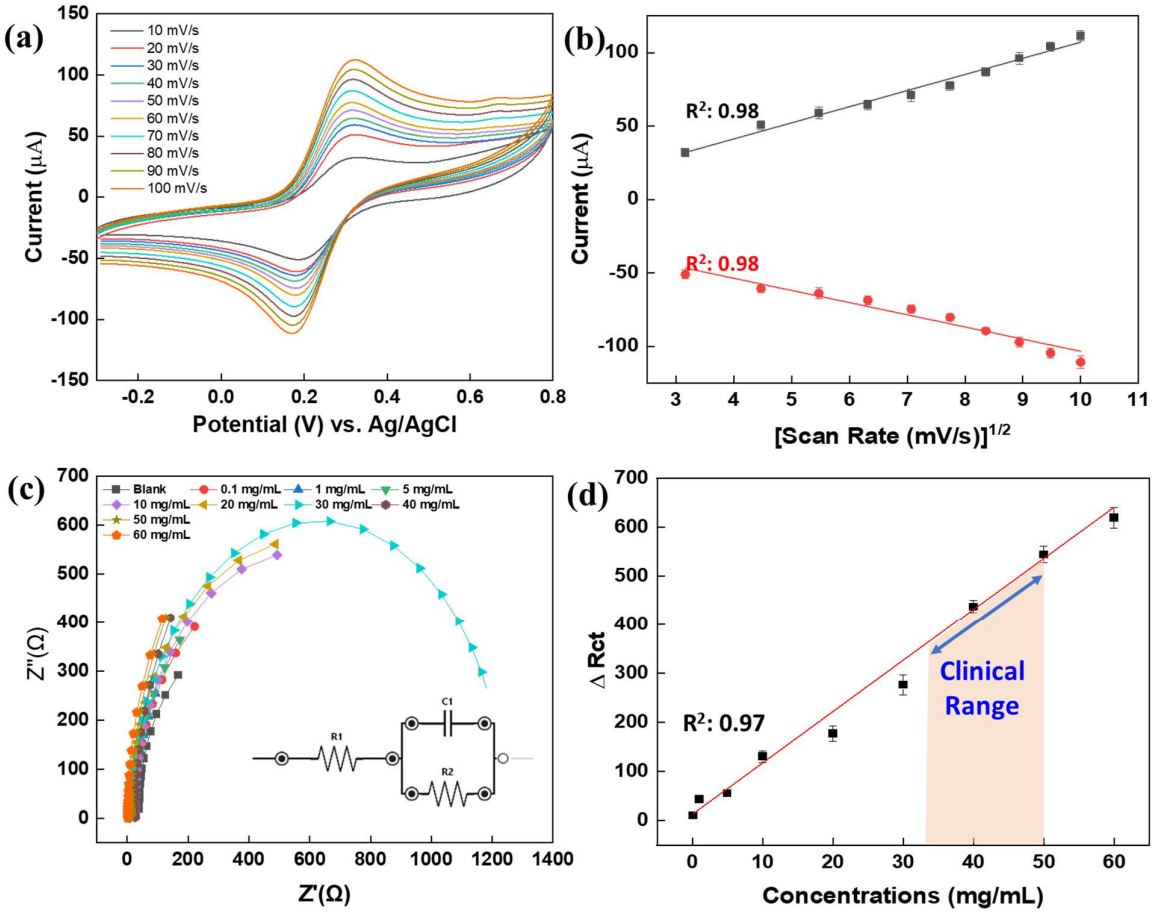

Figure 5.7: (a) *CV responses of the* anti-ALB/c-MWCNT/Co-MOF/GCE *immunosensor at varying scan rates in 5 mM ZS,* ***(b)*** *the corresponding linearity for anodic and cathodic peak current with a correlation coefficient (R^2) of 0.98,* ***(c)*** *EIS responses of the* anti-ALB/c-MWCNT/Co-MOF/GCE *sensor probe at different concentrations of ALB (0.1 - 60 mg/mL) in 5 mM ZS,* ***(d)*** *linear calibration curve of the response recorded with an R^2 value of 0.97*

A comparative evaluation of the developed sensing probe with recently developed electrochemical sensing surfaces is shown in **Table 5.2** reporting their composition, fabrication strategy, detection method, analytical performance (LDR and LOD), and real sample used.

Table 5.2: *Description of the recently developed electrochemical detection of albumin comparing their fabrication and analytical details (NR: Not reported)*

S. No.	Probe Configuration	Fabrication Strategy	Technique Used	Dynamic Range	LOD	Real Sample	Ref.
1.	CoTe/GCE	CoTe nanorods were synthesized using hydrothermal and then CoTe slurry was drop-casted on electrode surface	CV	NR	0.09 nM	Urine	[40]
2.	PDA/TiO_2 NPs/CPE	TiO_2 NPs were synthesized using sol-gel method and drop casted on CPE. Further, polydopamine (PDA) was electrodeposited on modified electrode	DPV	37 - 555 µM	10.3 µM	Drug Sample	[41]
3.	anti-HSA/Au@CGR-SPCE	Au@CGR composite was synthesized were by mixing gold nanoparticles and carboxylated graphene in a 1:3 ratio. Anti-HSA were immobilized	CA	2.5 - 500 µg/mL	1.5 µg/mL	Urine	[42]
4.	anti-HSA/CS/CuO NPs /ERGO/GCE	Cu was electrochemically deposited on reduced graphene modified electrode surface and then chitosan was drop-casted on electrode surface.	DPV	10 - 450 ng/mL	2.6 ng/mL	NR	[43]
5.	GE/AuNPs/PTH-MB/MIP	Polythionine-methylene blue was electro polymerized on AuNPs modified electrode and then MIP was synthesized using o-phenylenediamine and hydroquinone	DPV	10^{-10} - 10^{-4} g/L	3.0×10^{-11} g/L	Urine	[44]
6.	**anti-ALB/cMWCNT/Co-MOF/GCE**	**Carboxylated multiwalled carbon nanotubes nanocomposite with cobalt based MOF modified electrode was used for immobilization of antibodies**	**EIS**	**0.1 - 60 mg/mL**	**0.024 mg/mL**	**Serum**	**Thia work**

3.4 Interference Study

The selectivity study of the developed immunosensor for ALB was also studied in the presence of potential interfering molecules which are normally present in the serum sample. The fabricated sensing probe was treated with a wide range of molecules present in serum, including glucose, glutamine, ascorbic acid, creatinine, globulin, lysozyme, uric acid, cysteine, and ALB. The EIS spectra were recorded against each molecule, and the calculated ΔRct are plotted as histograms in **Figure 5.8(a)**.

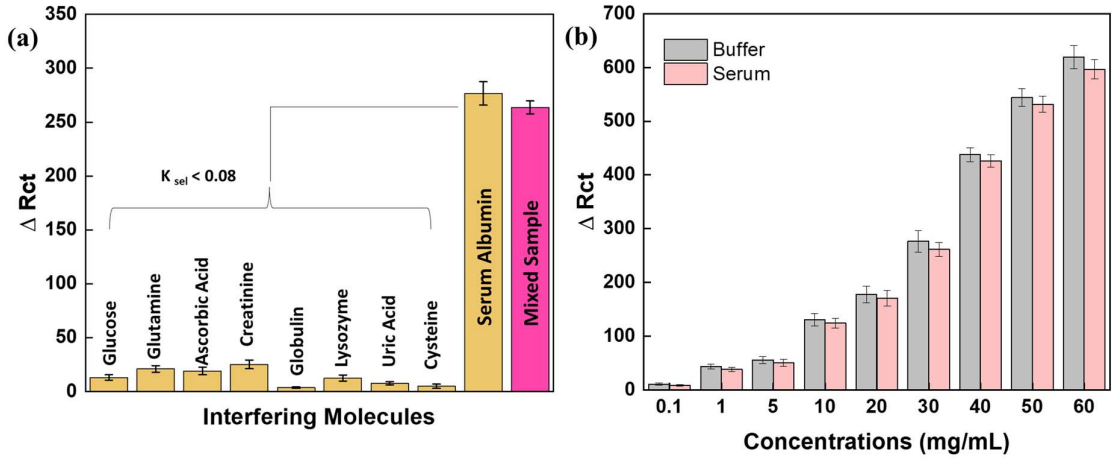

***Figure 5.8**: **(a)** Histogram representing the selectivity assay against interfering molecules, **(b)** Histogram depicting the final sensing probe's comparative responses in serum and buffer sample*

Additionally, the selectivity coefficient (K_{sel}) was also calculated using **equation 2** for each interfering molecule, and the respective values is represented in **Table 5.3.**

$$K_{Sel} = \frac{(Signal)_{interferent}}{(Signal)_{ALB}} \qquad \textbf{equation 2}$$

where K_{sel} depicts the selectivity coefficient, $(Signal)_{interferent}$ represents the response that corresponds to the interferents, and $(Signal)_{ALB}$ represents the response that corresponds to ALB.

The calculated K_{sel} was found to be less than 0.08, which helps establish the fact that the constructed sensor possesses high selectivity for the sensing of ALB. This selective response

of the final sensing probe was attributed to the highly selective immuno-complexation reaction occurring between the antibody (anti-ALB) and the antigen (ALB).

Table 5.3: *Description of interfering molecule along with their obtained ΔRct and their* K_{sel}

S. No.	Interfering Molecules	Δ Rct (Ω)	K_{sel}
1.	Glucose	13.1 (± 1.51)	0.04
2.	Glutamine	21.04 (± 1.19)	0.07
3.	Ascorbic Acid	19.06 (± 2.17)	0.06
4.	Creatinine	24.02 (± 2.34)	0.08
5.	Globulin	3.67 (± 0.68)	0.01
6.	Lysozyme	12.58 (± 1.87)	0.04
7.	Uric Acid	7.78 (± 1.16)	0.02
8.	Cysteine	4.91 (± 1.09)	0.01
9.	ALB	276.65 (± 6.14)	1

This also helps in establishing the facts that the immobilized antibody on the anti-ALB/c-MWCNT/Co-MOF/GCE sensing surface was biologically active and there is no chance of false signal generation. Additionally, the sensing probe was also tested against the mixed sample, where all the interferents were added with the target analyte and the EIS signal was recorded. It was observed that the created surface had a 95.2% efficacy in detecting ALB, even in the mixed sample **[**pink bar in **Figure 5.8(a)].**

3.5 Real Sample Analysis

The commercial applicability of the fabricated sensing surface is needed to be assessed for showing its application in the real sample. Serum albumin is a clinically proven marker of kidney disease; hence, the serum sample was selected as a real matrix for determining the analytical performance of the immunosensing probe in the complex environment. This study was conducted using the spike and recovery method, where the different known concentrations

of ALB were added in the serum sample, following equilibration with PBS. The anti-ALB/c-MWCNT/Co-MOF/GCE sensing surface was allowed to react with the spiked serum sample for 30 minutes, and then the EIS spectra were recorded for every subsequent concentration of ALB. The recovery percentage for the different concentrations of ALB was calculated using **equation 3.**

$$\%\ \boldsymbol{Recovery} = \frac{[X]_{ALB} - [Y]_{ALB}}{[Z]_{ALB}}\ \boldsymbol{x\ 100} \qquad \textbf{equation 3}$$

where $[Y]_{ALB}$ and $[X]_{ALB}$ represent the ALB concentrations for the blank and spiked samples, respectively; $[Z]_{ALB}$ represents the ALB concentrations in a standard buffer solution.

The increase in Rct value was recorded with an increase in concentrations of ALB in the real matrix, and this result corresponds to the binding of ALB on the final sensing probe. The calculated ΔRct value for the different concentrations of ALB in the serum matrix and the buffer are represented as a histogram in **Figure 5.8(b)**.

Table 5.4*: Description of the recovered ALB concentrations and % recovery using the developed sensor in serum matrix*

S. No.	Spiked Concentrations (mg/mL)	Recovered Concentrations (mg/mL)	% Recovery
1.	0.1	0.084(±0.002)	84.02
2.	1	0.87 (±0.03)	87.65
3.	5	4.52 (±0.18)	90.45
4.	10	9.51 (±0.57)	95.19
5.	20	19.18 (±1.85)	95.90
6.	30	28.33 (±1.79)	94.45
7.	40	38.93 (±1.37)	97.34
8.	50	48.79 (±2.16)	97.58
9.	60	57.76 (±2.30)	96.28

The linear regression equation of the obtained response in the serum matrix was represented as ΔRct (Ω) = 10.24 (±4.30) [conc. of ALB] + 9.92 (±0.43). The calculated LOD for the sensing probe in the real sample was found to be 0.026 mg/mL. These results established the fact that the developed sensing surface was capable of determining ALB in the human serum samples with recovery percentage of 84 - 97 % and thus can be used for practical analysis.

3.6 Reproducibility and Long-term Stability

The commercial viability of the developed probe was examined in terms of reproducibility and long-term stability by performing the experiments using protocols reported in the literature. Starting with the reproducibility test, the fabrication of anti-ALB/c-MWCNT/Co-MOF/GCE was performed on the five different electrode surfaces, keeping all the fabrication conditions the same. The obtained variation in the response of five different electrode surfaces was found to be less than 5.8%. This deviation corroborates the minor variation that might occur due to the handling error because the sensing surfaces were manually synthesized. Furthermore, the probe's long-term stability has been assessed by keeping the constructed electrode at 4 °C and recording its EIS spectra every week. The spectra were recorded for a period of 5 weeks, and it was observed that the sensing probe maintained its performance up to 88.13 % till 4 weeks. After this, decrement in response was recorded, which might occur due to the decrease in activity of the antibody over the electrode surface.

4. Conclusion

In this study, we have designed an innovative electrochemical immunosensor to track ALB in human serum samples. The immunosensing probe was designed by functionalizing the Co-MOFs-c-MWCNT nanocomposite with anti-ALB. After each sequential modification, the electrode surface was characterized using numerous techniques, including SEM, EDS, XPS, FTIR, and electrochemical methods. Following extensive characterizations, the analytical efficacy of the probe towards ALB was evaluated in both buffer and serum samples. This

nanocomposite provides the enhanced surface area for the functionalization of anti-ALB molecules on the electrode, and thus the fabricated probe was used for ALB detection. The probe detected ALB in a linear range of 0.1 to 60 mg/mL, covering its clinically pertinent concentrations. The developed sensor is intriguing because of its facile fabrication procedure, wide LDR, low LOD, and excellent selectivity for the analyte. This is the first study of its kind to employ a Co-MOFs-c-MWCNT nanohybrid immunosensing platform for ALB sensing. In the future, it could potentially serve as a valuable platform for personalized sensing and thus be employed in the healthcare sector for the diagnosis of kidney diseases.

References

[1] H.C. Zhou, J.R. Long, O.M. Yaghi, Introduction to metal-organic frameworks, Chem. Rev. 112 (2012) 673–674.

[2] A.E. Baumann, D.A. Burns, B. Liu, V.S. Thoi, Metal-organic framework functionalization and design strategies for advanced electrochemical energy storage devices, Commun. Chem. 2 (2019).

[3] Shubhangi, I. Nandi, S.K. Rai, P. Chandra, MOF-based nanocomposites as transduction matrices for optical and electrochemical sensing, Talanta. 266 (2024) 125124.

[4] Y. Hu, W. Li, Z. Wei, H. Yang, Y. Wang, S. Li, Advances in electrochemical sensing with ZIF-67 and related materials, Int. J. Electrochem. Sci. 18 (2023).

[5] N. Shubhangi, R. Kumari, S.K. Rai, P. Chandra, Electrochemical Assembly of Nickel Metal Organic Framework-Decorated Nanoimprinted Gold Dendrites as Peroxidase Mimic for High-Performance Hydrogen Peroxide Sensing, ACS Appl. Nano Mater. 7 (2024) 1388–1401.

[6] Z.A. Sandhu, M.A. Raza, N.S. Awwad, H.A. Ibrahium, U. Farwa, S. Ashraf, A. Dildar, E. Fatima, S. Ashraf, F. Ali, Metal-organic frameworks for next-generation energy storage devices; a systematic review, Mater. Adv. 5 (2023) 30–50.

[7] R.F. Mendes, F. Figueira, J.P. Leite, L. Gales, F.A. Almeida Paz, Metal-organic frameworks: A future toolbox for biomedicine?, Chem. Soc. Rev. 49 (2020) 9121–9153.

[8] J.P. Leite, F. Figueira, R.F. Mendes, F.A. Almeida Paz, L. Gales, Metal-Organic Frameworks as Sensors for Human Amyloid Diseases, ACS Sensors. 8 (2023) 1033–1053.

[9] M. Shams, Z. Niazi, M.R. Saeb, S. Mozaffari Moghadam, A.A. Mohammadi, M. Fattahi, Tailoring the topology of ZIF-67 metal-organic frameworks (MOFs) adsorbents to capture humic acids, Ecotoxicol. Environ. Saf. 269 (2024).

[10] Y. Hu, X. Song, Q. Zheng, J. Wang, J. Pei, Zeolitic imidazolate framework-67 for shape stabilization and enhanced thermal stability of paraffin-based phase change materials, RSC Adv. 9 (2019) 9962–9967.

[11] G. Ebube Uwaya, K. Bisetty, A sensitive ZIF-67/ MWCNTs composite-based sensor for the detection of sunset yellow in food and beverages, J. Electroanal. Chem. 951 (2023).

[12] G. Zhong, D. Liu, J. Zhang, The application of ZIF-67 and its derivatives: Adsorption, separation, electrochemistry and catalysts, J. Mater. Chem. A. 6 (2018) 1887–1899.

[13] T. Shi, S. Hussain, C. Ge, G. Liu, M. Wang, G. Qiao, ZIF-X (8, 67) based nanostructures for gas-sensing applications, Rev. Chem. Eng. 39 (2023) 911–939.

[14] R. Gallegos-Monterrosa, R.O. Mendiola, Y. Nuñez, C. Auvynet, K.M. Kumar, B. Tang, L.I. Ruiz-Ortega, V.H. Bustamante, Antibacterial and antibiofilm activities of ZIF-67, J. Antibiot. (Tokyo). 76 (2023) 603–612.

[15] F.S. Butt, M. Safdar, A. Lewis, N.A. Mazlan, N. Radacsi, X. Fan, H. Arellano-García, Y. Huang, Superhydrophobic ZIF-67 with exceptional hydrostability, Mater. Today Adv. 20 (2023).

[16] D. Eskiköy Bayraktepe, Z. Yazan, Application of Single-use Electrode Based on Nano-clay and MWCNT for Simultaneous Determination of Acetaminophen, Ascorbic Acid and Acetylsalicylic Acid in Pharmaceutical Dosage, Electroanalysis. 32 (2020) 1263–1272.

[17] S. Biswas, S.S. Panja, S. Bose, The long-range π-conjugation between electron-rich species and multiwall carbon nanotubes influences the fluorescence lifetime and electromagnetic shielding, Nanoscale Adv. 2 (2020) 4464–4472.

[18] Y. Wang, Z. Gao, Y. Shang, Z. Qi, W. Zhao, Y. Peng, Proportional modulation of zinc-based MOF/carbon nanotube hybrids for simultaneous removal of phosphate and emerging organic contaminants with high efficiency, Chem. Eng. J. 417 (2021).

[19] H. Li, Q. Yao, J. Fan, J. Du, J. Wang, X. Peng, An NIR fluorescent probe of uric HSA for renal diseases warning, Dye. Pigment. 133 (2016) 79–85.

[20] Divya, P. Chandra, Bioengineered cellulosic paper micro-device for serum albumin detection in clinical range, Int. J. Biol. Macromol. 258 (2024) 128921.

[21] T. Chen, N. Xie, L. Viglianti, Y. Zhou, H. Tan, B.Z. Tang, Y. Tang, Quantitative urinalysis using aggregation-induced emission bioprobes for monitoring chronic kidney disease, Faraday Discuss. 196 (2017) 351–362.

[22] A. Sammi, Divya, S. Mahapatra, R. Kumar, P. Chandra, Nano-Bio-engineered Silk Matrix based Devices for Molecular Bioanalysis, Biotechnol. Bioeng. (2021).

[23] M.O. Shaikh, P.Y. Zhu, C.C. Wang, Y.C. Du, C.H. Chuang, Electrochemical immunosensor utilizing electrodeposited Au nanocrystals and dielectrophoretically trapped PS/Ag/ab-HSA nanoprobes for detection of microalbuminuria at point of care, Biosens. Bioelectron. 126 (2019) 572–580.

[24] U.P. Azad, P. Chandra, Handbook of Nanobioelectrochemistry: Application in Devices and Biomolecular Sensing, Handb. Nanobioelectrochemistry Appl. Devices Biomol. Sens. (2023) 1–950.

[25] K. Omidfar, A. Dehdast, H. Zarei, B.K. Sourkohi, B. Larijani, Development of urinary albumin immunosensor based on colloidal AuNP and PVA, Biosens. Bioelectron. 26 (2011) 4177–4183.

[26] V. Borse, P. Chandra, R. Srivastava, eds., BioSensing, Theranostics, and Medical Devices, BioSensing, Theranostics, Med. Devices. (2022).

[27] E. Saeb, K. Asadpour-Zeynali, A novel ZIF-8@ZIF-67/Au core–shell metal organic framework nanocomposite as a highly sensitive electrochemical sensor for nitrite determination, Electrochim. Acta. 417 (2022) 140278.

[28] Divya, P. Chandra, ZIF-67-MWCNT Nanohybrid Based Electrochemical

Immunosensing Device for Diagnosing Kidney Dysfunction, Proc. IEEE Sensors. (2023).

[29] N.L. Torad, R.R. Salunkhe, Y. Li, H. Hamoudi, M. Imura, Y. Sakka, C.C. Hu, Y. Yamauchi, Electric Double-Layer Capacitors Based on Highly Graphitized Nanoporous Carbons Derived from ZIF-67, Chem. – A Eur. J. 20 (2014) 7895–7900.

[30] X. Li, Z. Niu, J. Jiang, L. Ai, Cobalt nanoparticles embedded in porous N-rich carbon as an efficient bifunctional electrocatalyst for water splitting, J. Mater. Chem. A. 4 (2016) 3204–3209.

[31] M. Al Murisi, S. Al-Asheh, M.A. Abdelkareem, A. Aidan, K. Elsaid, A.G. Olabi, In situ Growth of Zeolite Imidazole Frameworks (ZIF-67) on Carbon Cloth for the Application of Oxygen Reduction Reactions and Microbial Fuel Cells, ACS Omega. 8 (2023) 44514–44522.

[32] H. Soleimani, M.K. Baig, N. Yahya, L. Khodapanah, M. Sabet, B.M.R. Demiral, M. Burda, Impact of carbon nanotubes based nanofluid on oil recovery efficiency using core flooding, Results Phys. 9 (2018) 39–48.

[33] X. He, X. Xu, G. Bo, Y. Yan, Studies on the effects of different multiwalled carbon nanotube functionalization techniques on the properties of bio-based hybrid non-isocyanate polyurethane, RSC Adv. 10 (2020) 2180–2190.

[34] M.Y. Sun, H. Xu, Y.T. Meng, X.M. Chen, M. Lu, H. Yu, C.B. Zhang, Facile design and synthesis of a nickel disulfide/zeolitic imidazolate framework-67 composite material with a robust cladding structure for high-efficiency supercapacitors, RSC Adv. 12 (2022) 23912–23921.

[35] X.H. Li, P. He, T. Wang, X.W. Zhang, W.L. Chen, Y.G. Li, Keggin-Type Polyoxometalate-Based ZIF-67 for Enhanced Photocatalytic Nitrogen Fixation, ChemSusChem. 13 (2020) 2769–2778.

[36] A.G. Dymerska, B. Środa, B. Zielińska, E. Mijowska, In situ insight into the low-temperature promotion of ZIF-67 in electrocatalytic oxygen evolution reaction, Mater. Des. 226 (2023) 111637.

[37] H. Chen, X. Wu, R. Zhao, Z. Zheng, Q. Yuan, Z. Dong, W. Gan, Preparation of reduced graphite oxide loaded with cobalt(II) and nitrogen co-doped carbon polyhedrons from a metal-organic framework (type ZIF-67), and its application to electrochemical determination of metronidazole, Microchim. Acta. 186 (2019) 1–9.

[38] Y. Ding, X. Zhao, P. Wu, R. Wang, L. Xie, Z. Li, Z. Zhu, H. Zhao, M. Lan, ZIF-67 MOF derived Co-Based CeO2 electrochemical sensor for dopamine, Electrochim. Acta. 463 (2023) 142802.

[39] X. Han, K. Cao, Y. Yao, J. Zhao, C. Chai, P. Dai, A novel electrochemical sensor for glucose detection based on a Ti3C2Tx/ZIF-67 nanocomposite, RSC Adv. 12 (2022) 20138–20146.

[40] U. Saeed, B. Fatima, D. Hussain, R. Ashiq, M. Naeem Ashiq, M. Najam-ul-Haq, CoTe nanorods based electrochemical sensor for quantitative detection of albumin from chronic kidney disease patients, J. Electroanal. Chem. 906 (2022) 115999.

[41] N. Zare, M. Shojaei, M.A. Taher, E.A. Afshar, M. Ghalkhani, G.G. Raja, F. Karimi, Electrochemical Sensor of Human Serum Albumin Bio-analyte Prepared Utilizing a Thin Film of Polydopamine/TiO2 Nanoparticles: Experimental and Docking Theoretical Investigations, Top. Catal. (2024) 1–10.

[42] V. Stanković, S. Đurđić, M. Ognjanović, B. Antić, K. Kalcher, J. Mutić, D.M. Stanković, Anti-human albumin monoclonal antibody immobilized on EDC-NHS functionalized carboxylic graphene/AuNPs composite as promising electrochemical HSA immunosensor, J. Electroanal. Chem. 860 (2020) 113928.

[43] B. Feyzi-barnaji, B. Darbasizadeh, E. Arkan, H. Salehzadeh, A. Salimi, F. Nili, R.

Dinarvand, A. Mohammadi, Immunoreaction-triggered diagnostic device using reduced graphene oxide/CuO NPs/chitosan ternary nanocomposite, toward enhanced electrochemical detection of albumin, J. Electroanal. Chem. 877 (2020) 114642.

[44] G. Zhang, Y. Yu, M. Guo, B. Lin, L. Zhang, A sensitive determination of albumin in urine by molecularly imprinted electrochemical biosensor based on dual-signal strategy, Sensors Actuators B Chem. 288 (2019) 564–570.